



# On the strength improvement of lightweight fibre networks by polymers, fibrils and fines

Tiina Pöhler · Jukka A. Ketoja · Timo Lappalainen · Veli-Matti Luukkainen · Ilkka Nurminen · Panu Lahtinen · Katariina Torvinen

Received: 28 June 2019 / Accepted: 21 May 2020 / Published online: 28 May 2020  
© The Author(s) 2020

**Abstract** Novel lightweight cellulose fibre materials containing various strength enhancing polymeric and fibrillar components were formed with the help of foam technology. Increasing inter-fibre bond strength and local material density was attempted with unique lignin-containing wood fines (V-fines), cellulose microfibrils (CMF), TEMPO-oxidized cellulose nanofibrils (TCNF), and macromolecules such as cationic starch, polyvinyl alcohol (PVA), and locust bean gum (LBG). The investigated fibres included both long hemp bast fibres and northern bleached softwood Kraft pulp. In the low-density range of 38–52 kg/m<sup>3</sup>, the compression stress and modulus were highly sensitive to inter-fibre bond properties, the multi-scale features of the fibre network, and the foaming agent employed. Still, the compression-stress

behaviour in most cases approached the same theoretical curve, derived earlier by using a mean-field theory to describe the deformation behaviour. At 10% addition level of fine components, the specific compression stress and compression modulus increased in the order of V-fines < CMF < TCNF. A tremendous increase in the compression modulus was obtained with LBG, leading to a material surface that was very hard. In general, the foams made with PVA, which acts both as foaming agent and reinforcing macromolecule, led to better strength than what was obtained with a typical anionic sodium dodecyl sulphate surfactant. Strength could be also improved by refining the softwood pulp.

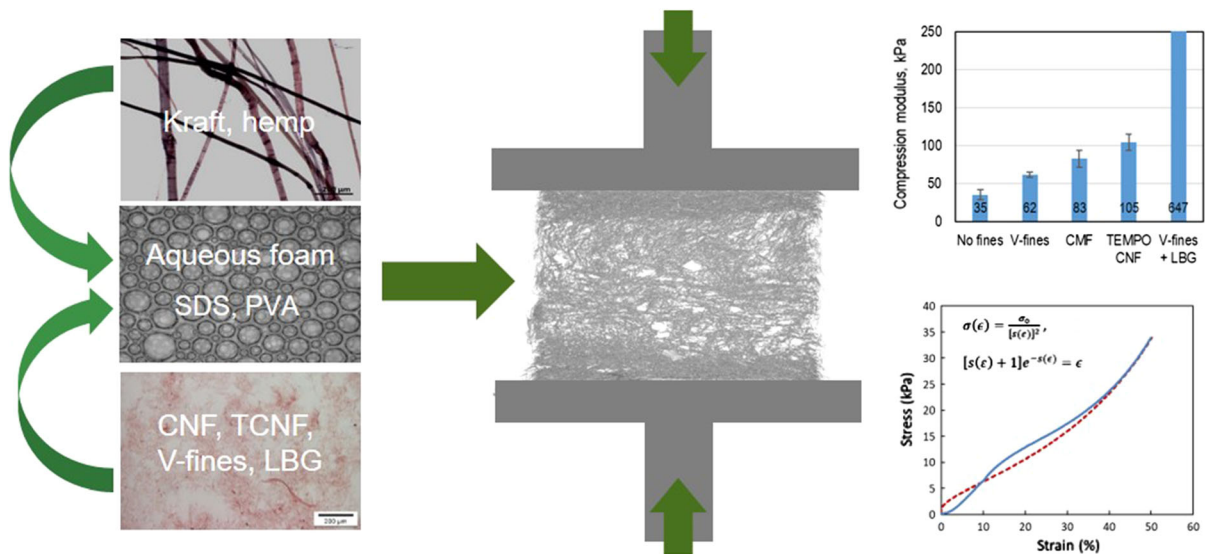
---

**Electronic supplementary material** The online version of this article (<https://doi.org/10.1007/s10570-020-03263-x>) contains supplementary material, which is available to authorized users.

---

T. Pöhler (✉) · J. A. Ketoja · T. Lappalainen · V.-M. Luukkainen · I. Nurminen · P. Lahtinen · K. Torvinen  
Solutions for Natural Resources and Environment, VTT  
Technical Research Centre of Finland Ltd, P.O. Box 1000,  
02044 Espoo, Finland  
e-mail: tiina.pohler@vtt.fi

## Graphic abstract



**Keywords** Foam forming · Cellulose nanofibril · Wood fines · Fibre · Softwood · Hemp · Polyvinyl alcohol · Locust bean gum · Compression test · Stress · Strain · Model

## Introduction

New low-density cellulose-based fibre materials made with the foam forming technique have recently been introduced as potential solutions to replace oil-based fibrous or foamed materials (Poranen et al. 2013; Madani et al. 2014). Feasible applications can be found in air filtration (Jahangiri et al. 2014), thermal insulation (Jahangiri et al. 2014; Pöhler et al. 2017), in acoustic control as sound absorption material (Jahangiri et al. 2016; Pöhler et al. 2016), and as cushioning material in packaging (Luo et al. 2017; Paunonen et al. 2018). These new lightweight materials are made by mixing fibres with aqueous wet foam generated with the help of a foaming agent (Al-Qararah et al. 2015a). The bubbles in the foam support fibres until drying so that a highly porous, deformable fibre network is formed. Rather little is known about the structure-strength relationship of these “fibre foams”, despite several recent experimental studies (Alimadadi and Uesaka 2016; Burke et al. 2019; Ketoja et al. 2019) and model simulations using

idealized fibre systems (Alimadadi et al. 2018; Hossein et al. 2019). The material characterization is challenging as strength can depend on the structural features in several size scales. These include the overall material network geometry, fibre properties (size distribution and flexibility) and the bonding ability of the fibres (total bond area and bond strength) (Alava and Niskanen 2006). Moreover, strength is a physical property that is not necessarily determined by the average structure but rather by structural heterogeneity affecting both stress concentration and local load-carrying capacity. For that reason, the deformation behaviour can be sensitive to the size distribution of fibres and fine components. With optimal combination and distribution of raw materials, it is possible to increase compression strength through local load-bearing regions without deteriorating large-scale material homogeneity. Current paper investigates this question applying a selected set of raw materials that have an exceptionally wide variety of characteristic sizes.

There is vast literature (Alava and Niskanen 2006; Picu 2011) on the strength properties of fibre networks in the medium density range of 300–1000 kg/m<sup>3</sup>, where the number of inter-fibre joints per fibre is large. The number of joints is proportional to the square of total fibre length in unit volume (Komori and Makishima 1977). Thus, with decreasing density, the number of joints per fibre and the relative bonded area

are greatly reduced. In such a situation, network deformations become non-affine (Picu 2011), so that local strains can differ greatly from the average behaviour. Moreover, the role of structural variations increases with reduced material density. With a low relative bonded area of a fibre network, heterogeneity of fibres becomes essential as well. The segment lengths between inter-fibre joints become longer [mean segment length can be 5–40 times greater than the fibre diameter (Ketoja et al. 2019)], and weak points along a fibre are not necessarily supported by other neighbouring fibres. Such features become increasingly important for compressive loads, for which a local network failure can simply mean that the associated fibre segment loses partly its ability to carry stress. This may happen not only by fibre bending, as shown in many previous models (Subramanian and Picu 2011; Bergström et al. 2019), but also by sudden buckling or displacement of an individual fibre under compressive stress (Ketoja et al. 2019). This was noticed experimentally by Ketoja et al. (2019), who found abrupt displacements in fibre networks using an image cross-correlation technique. The possibility of a localizing failure in a heterogeneous fibre has been omitted in previous simulation models (Alimadadi et al. 2018; Hossain et al. 2019; Bergström et al. 2019), which are based on uniform fibre segments without inherent structural unevenness inside a single segment between two joints. Ketoja et al. (2019) introduced a mean-field theory where the buckling of fibre segments was postulated to be an important deformation mechanism describing mean stress build-up during network compression. The theory explained the stress increase for intermediate compressive strains in varied well-bonded fibre materials in the density range of 20–100 kg/m<sup>3</sup>. Mäkinen et al. (2020) provided further evidence for the theory by showing that acoustic energy emission could be directly correlated with the stress-compression behaviour. Their cyclic measurements revealed another source of acoustic events than fibre bending. However, the theory was not able to explain the behaviour at very large strains because of collective softening of the material (Picu and Subramanian 2011). Moreover, the theory overestimated the stress when the strain was below 10% (Ketoja et al. 2019; Mäkinen et al. 2020) and when large amounts of cellulose microfibrils (CMF) were added to a fibre network (Ketoja et al. 2019). Added CMF seemed to increase strength at

intermediate compression levels by forming cellulose micro-scale sheets within the fibre network (Bossu et al. 2019).

In the current study, we have taken the above considerations into account when improving the strength of lightweight natural fibre materials. The bond strength and total inter-fibre contact area (Sormunen et al. 2019) can be increased with polymeric, fibrillar and fines materials. The strengthening mechanisms are twofold: Firstly, fine components can build loose material bridges between fibres, which, during drying with the help of surface tension forces, drag fibres in contact with one another thus increasing the number of bonds and reducing the mean fibre segment length. Usually, this is associated with a higher density of the whole material as well. Secondly, polymeric and fibrillar components can strongly affect the strength of individual bonds by (a) enhancing the mechanical entanglement of the inter-fibre fibrils, (b) creating a larger microscopic contact area where short-range interactions become effective, or (c) by changing these chemical forces (Schmied et al. 2013). Overall material strength is further improved if the formed network is able to distribute local stresses evenly over the fibre network. For this reason, we explored multi-scale network structures by combining wood and hemp fibres with varying dimensions and flexibilities. The studied fibre and fine components covered the broad length (width) range from  $\sim 40 \mu\text{m}$  ( $\sim 3 \text{ nm}$ ) up to  $\sim 15 \text{ mm}$  ( $\sim 50 \mu\text{m}$ ). In addition to strength measurements, the micro-scale homogeneity of the structures was followed as well.

## Materials and methods

### Fibres and fine components

Hemp bast fibres were selected as the long fibre component in the furnish. The fibre length of a single hemp bast fibre can vary from 1 to 34 mm (average 8–14 mm) with a diameter between 17 and 23  $\mu\text{m}$  (Shahzad 2012). The typical value of the longitudinal Young's modulus of a hemp fibre is 30–60 GPa (Shahzad 2012). Finnish hemp bast fibres (Cannabis sativa, delivered by HempRefine Oy) with the chemical composition of 81% cellulose, 11% hemicellulose, and 5% lignin were treated with a Kvarn BAHS-30 hammer mill (Kamas Industri AB). Fibres were

inserted into the mill and let to rotate until they fell through a 15 mm slot screen. The milling process enhanced the separation of fibres from fibre bundles, see Fig. 1. The treated fibres were further processed to increase their bonding ability with a soda cooking process. The cooking time was 90 min at 165 °C. The total alkali (NaOH) was 4 mol/kg. The liquid to solid ratio was 7.5, the yield was 70.5%, and the kappa number was 6.0.

The medium-size fibre component was Northern Bleached Softwood Kraft (NBSK) pulp (Metsä-Fibre Oyj, Äänekoski, Finland) with an average length-weighted fibre length of 2.1 mm and fibre width 28 µm. Both unrefined (ur) and refined (r) pulps were used. The refining was done with a Voith Sulzer laboratory refiner at KCL Oy, Finland, using conical discs. The pulp consistency in the refining was 4%, and the specific edge load was 2.5 J/m. The refining was stopped at the specific energy consumption of 100 kWh/t. The SR number of the refined pulp was 18.7. The chemical composition of NBSK pulp has been reported to be 85% cellulose, 14% hemicellulose, and 1% lignin (Lahtinen et al. 2014a) and Young's modulus of NBSK fibre ~ 40 GPa by Neagu et al. (2006).

Three different wood- and Kraft-cellulose-originated fine components were employed in the furnishes: V-fines, cellulose microfibrils (CMF), and TEMPO ((2,2,6,6-tetramethylpiperidin-1-yl)oxyl) oxidized cellulose nanofibrils (TCNF). Lignocellulosic V-fines were produced directly from fresh

softwood (*Picea Abies*) using a laboratory grinder equipped with a unique grinding stone designed for fines production in atmospheric conditions (Nurminen et al. 2018). A grinding stone with 70 mesh grits (Norton A701-L12VGP) and a serrated V-shape surface was employed. The angle between the apparent fibre alignment and the serrated surface was 15 degrees. The wood feed was 0.9 mm/s and stone velocity 20 m/s. The estimated energy consumption was 2 MWh/t. The fibrillated material was screened through a 14-mesh wire. The population average fibre length was 0.18 mm, and over 70% of the measured particles had a length below 0.2 mm.

The two different fibrillated cellulose grades were produced from a never-dried NBSK. The production of the coarser CMF was started by soaking the pulp at 2% consistency and dispersing it with a high-shear Ystral X50/10 Dispermix mixer for 30 min at 2000 rpm. The pulp suspension was fibrillated in a grinder (Supermasscolloider MKZA10-15J, Masuko Sangyo Co., Japan) at 1500 rpm. Fibrillated material was obtained after six passes through the grinder. The fibre slurry turned into a homogeneous, white and viscous gel after the grinding with a final solid content of 2.2%. The apparent viscosity at a shear rate of 10 1/s was 0.68 Pas, measured according to the method described by Lahtinen et al. (2014b).

A more anionic and nano-sized TCNF was produced according to the method described by Skogberg et al. (2017). The outcome was a viscous and transparent hydrogel with a final dry matter content

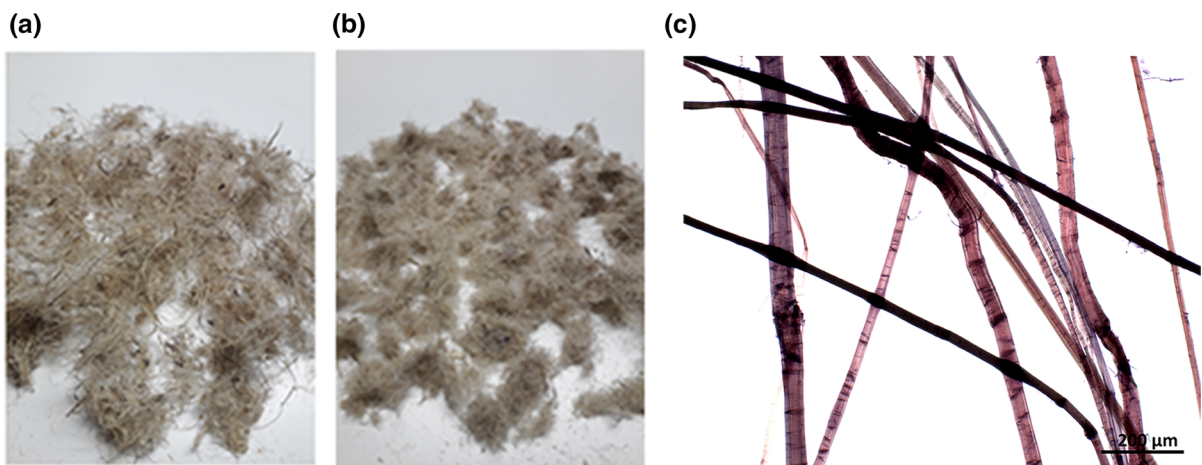


**Fig. 1** Photographs of **a** untreated hemp bast fibres, **b** milled hemp bast fibres, and **c** optical microscope image of macerated and stained (Herzberg stain) hemp bast fibres

of 1.08% and a charge value of approximately 1 mmol/g dry pulp. The apparent viscosity at the shear rate 10 1/s was 2.48 Pas. Optical micrographs of the different fine components are shown in Fig. 2 and scanning electron microscope (SEM) micrographs in Fig. 3.

Figure 4 shows an estimated size scale of the employed fibre and fine components based on microscopy. The fibre width was spread over 5 and the fibre length over 4 orders of magnitude. The foam-aided material formation was able to handle the large size differences among the raw materials.

#### Hydrocolloidal and water-soluble polymers

Locust bean gum (LBG), a galactomannan obtained from the seed endosperm of the carob tree (i.e. *Ceratonia siliqua*), was obtained from Sigma-Aldrich. LBG is widely utilized as an additive in various industries such as food, pharmaceuticals, paper, textile, oil well drilling, and cosmetics (Barak and Mudgil 2014). It is a straight chain polymer of mannose with one galactose branch on every fourth mannose and has an average molecular weight of approx. 310 000 g/mol (Barak and Mudgil 2014). Industrial applications of LBG are based on its ability to form hydrogen bonding with water molecules. LBG was added as a powder into the foam at room temperature. According to Barak and Mudgil (2014), LBG is partially soluble in cold water.

The conventional cationic wet end starch Raisamyl 50021 (DS = 0.035) was employed mainly for ensuring high retention of the CMF and the strongly negatively charged TCNF in particular.

#### Foaming agents

Two different foaming agents were applied: anionic sodium dodecyl sulphate,  $\text{NaC}_{12}\text{H}_{25}\text{SO}_4$ , SDS (Sigma-Aldrich) with 90% purity, and polyvinyl alcohol PVA (Poval Kuraray). PVA is a linear water-soluble synthetic polymer that inherently creates a suitable type of foam for the foam-forming process. On the other hand, PVA is a strong binder: it is 3–4 times stronger than starch and 2–3 times stronger than acrylic or PVAc-based latexes (Miller et al. 1998; Finch 1992). The molecular weight of PVA usually varies between 15,000 and 250,000 g/mol. This weight is much higher than that of small anionic surfactants (e.g. the molecular weight of SDS is about 288 g/mol) but smaller than the molecular weight of LBG. PVA grades 6–88 (partially hydrolysed,  $M_w \sim 37,000$  g/mol) and 28–99 (fully hydrolysed,  $M_w \sim 145,000$  g/mol) were applied. Since the foaming of grade 28–99 was fairly poor, a blend with better foaming 6–88 was employed to optimize foaming efficiency and binding effect. Both SDS and PVA foaming agents are readily biodegradable.

#### Foam generation and forming

Water, a foaming agent (SDS or PVA blend), and the furnish components were mixed in a cylindrical vessel. CMF and TCNF were mixed with the fibre suspension before the surfactant was added and before foaming. Cationic starch, when applied, was mixed with the pulp slurry approximately 30 s before the foaming agent was added. Foam generation was continued until the air content of the fibre foam

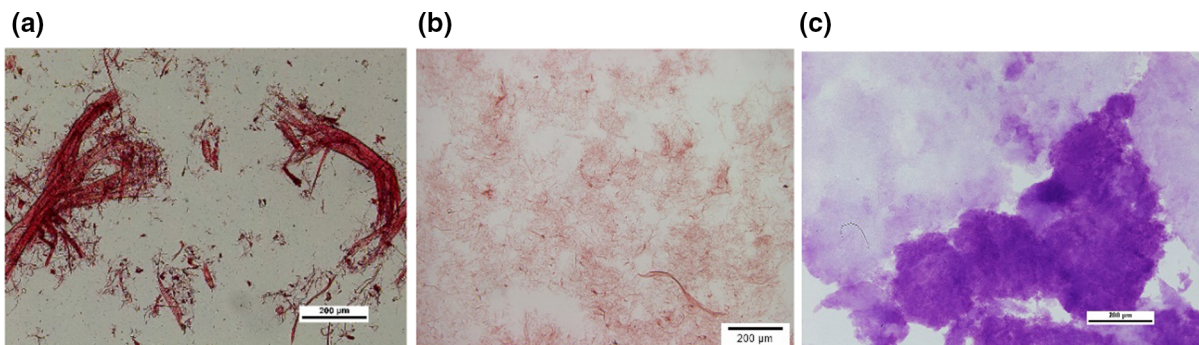


**Fig. 2** Optical micrograph images of **a** V-fines, **b** CMF, and **c** TCNF. V-fines and CMF were stained with Congo red, and TCNF was stained with toluidine blue. The measure bar shows the length of 200 µm

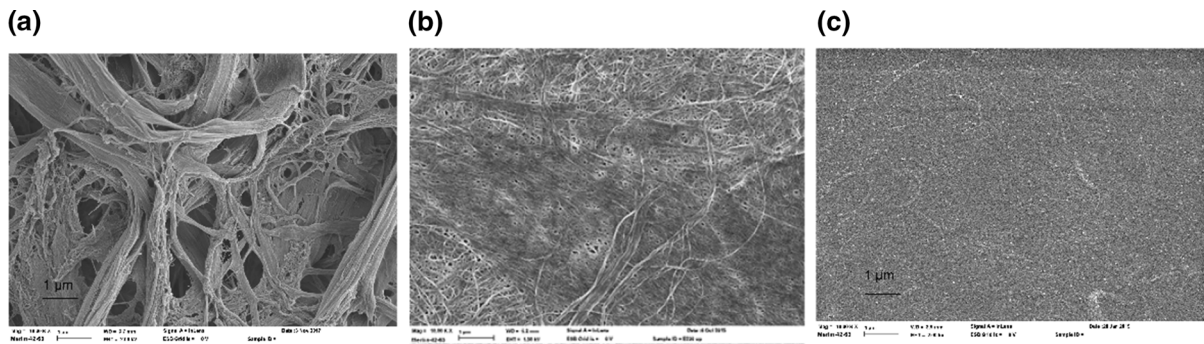


**Fig. 3** SEM images of **a** V-fines, **b** CMF, and **c** TCNF using equal magnification to illustrate the size difference between the components. The measure bar shows the length of 1  $\mu\text{m}$

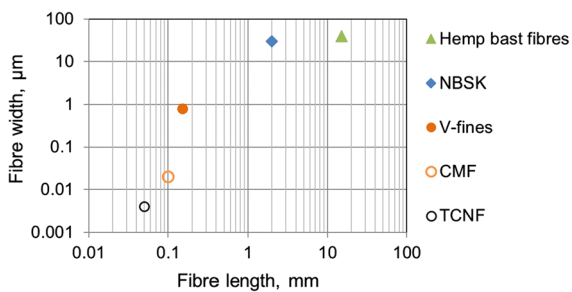


**Fig. 4** Estimated size scale of the fibre and fine components employed based on microscopy

reached the target of 50–60%. The fibre foam was poured along a plate into a deep mould with a wire bottom, drained by gravity for 15 min, and removed from the mould on the wire. The wet material (dry matter content around 12%) was inserted into a laboratory oven and dried at 70 °C. Drying to a remaining moisture content below 10% was complete within 24 h. In a special trial point (TP11) made with LBG, the drainage was extremely slow. Therefore, the samples were dried in the oven at a higher temperature (100 °C). Table 1 shows the most essential foaming parameters for the trial points.

The final material density level was adjusted by pressing the wet foam after the drainage of the free water and/or after the drying of the material. The once-dried materials were rewetted with water to the dry matter content of 50% and pressed between two plates with spacers to the desired final thickness and dried again in an oven (70 °C). Both panel surfaces were densified due to the dewatering in one direction and the pressing procedures. The bulk density values presented in the Tables 2 and 3 are the average density

values of the materials. Photographs of foam-formed fibre materials are shown in Fig. 5.

In thin foam-formed sheets obtained by removing the foam by vacuum, fibres usually orient themselves mainly to the planar direction, in parallel to the foam flow (Järvinen et al. 2018). It is not obvious that similar preferred orientation could be found inside thick fibre networks drained by gravity. In addition to foam flow and drainage, the orientation may also depend on the air content and bubble size and employed raw materials together with boundary effects caused by the mould walls. Tomography images were produced to capture possible preferred fibre orientations in the formed materials.

#### Material testing methods

Basis weight was measured by weighing the material at 50% RH and 23 °C and by measuring the material dimensions. Thickness was measured with a laser beam. Compression stress was measured with universal material tester (Lloyd) at 10% deformation, according to EN 826 (2013). The compression test was continued to 50% deformation level after 1 min of relaxation. Compression modulus was defined from the slope of the stress–strain curve in the elastic (linear) deformation region. Specific compression stress was defined by dividing the compression stress with density. Materials were imaged with a tomographic scanner (RX Solutions, France). Tube voltage 40 kV and current 300  $\mu\text{A}$  were used. The voxel size was 25  $\mu\text{m}$ .

**Table 1** Foaming parameters for the trial points

	TP1–TP10	TP11 (LBG)
Diameter of the cylindrical foaming tank (cm)	32	16
Mixing speed (rpm)	3000	3500
Initial volume of the pulp suspension (l)	6.8	0.93
Fibre consistency in pulp suspension before foaming (%)	2	2.7
Air content after foaming (%)	58–62 (SDS) 56–63 (PVA blend)	63
SDS concentration (%)	0.12	0.06
PVA concentration (%)	0.1 (6–88) and 0.5 (28–99)	–
Mould dimensions (cm)	42 × 42	9.8 (diameter)
Density adjustment	Pressing of wet foam + rewetting and pressing	Pressing of wet foam

The furnish composition of TP1–TP6 are specified in Table 2 and TP7–TP11 in Table 3

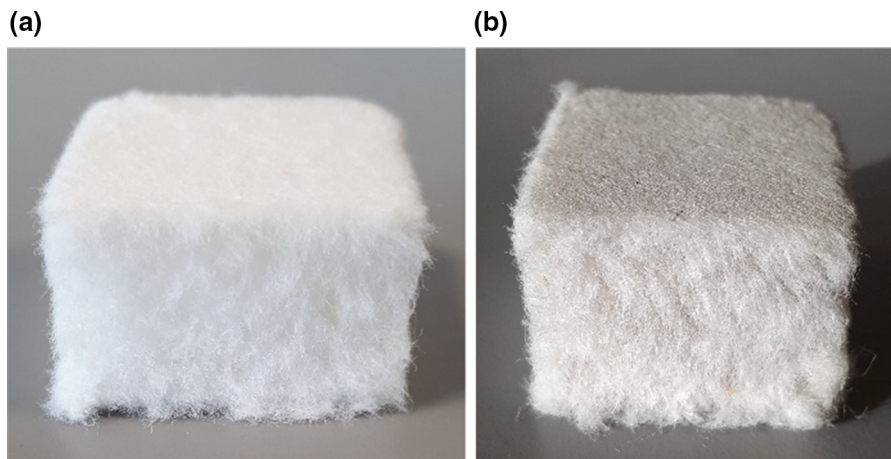


**Fig. 5** Photographs of the foam-formed materials, **a** 100% unrefined NBSK foamed with PVA (TP4) and **b** refined NBSK and hemp foamed with SDS (TP3), see Table 2. The sawn material pieces are of size 30 × 30 × 20 mm

### Theoretical analysis

The analysis of the experimental results is based on the following postulates on relevant mechanisms: (1) under compressive load, deformation of very porous material begins with bending of surface and other slender fibre segments (Subramanian and Picu 2011) and closing up of the largest voids and gaps of the material. (2) Gradually, at higher strains, local axial stresses build up (Subramanian and Picu 2011), especially in regions where a fibre or several of them resist bending. This resistance may be caused by the local orientation of fibres, their geometry (e.g. large cross-sectional area), internal stresses or by high local network density. (3) At certain points, the stress can

become high enough to trigger a sudden (buckling) failure in a fibre segment. Because of the inherent heterogeneity of the fibres, their failures can deviate significantly from the classical Eulerian buckling. Besides buckling of the whole segment, a localized failure in a fibre wall is possible as well (Mäkinen et al. 2020). In any case, if such a failure happens, the stress is re-distributed quickly to other resisting regions. Thus, the development of local deformations can be quite heterogeneous.

Ketoja et al. (2019) derived simple equations for a situation where free fibre segments buckle (with critical load proportional to the inverse square of segment length) and describe the stress-compression behaviour. Their theory assumed exponentially

**Table 2** Basic material properties of the foam-formed materials without added fine components

TP#	Foaming agent	Furnish			Density (kg/m <sup>3</sup> )	Stress (kPa, 10%)	Stress (kPa, 50%)	$\frac{1}{\sigma} \frac{d\sigma}{d\epsilon}$ at 50%
		NBSK ur	NBSK r	Hemp				
1	SDS	100			41.0	3.1 ± 0.1	18.3 ± 0.1	4.39 ± 0.08
2	SDS		100		43.6	4.7 ± 0.1	24.5 ± 0.1	4.24 ± 0.26
3	SDS		80	20	38.7	3.1 ± 0.5	20.6 ± 0.8	3.77 ± 0.13
4	PVA	100			43.4	5.2 ± 0.9	22.3 ± 2.6	3.79 ± 0.26
5	PVA		100		44.5	9.8 ± 0.7	31.8 ± 2.1	2.96 ± 0.19
6	PVA		80	20	45.0	12.6 ± 1.9	37.8 ± 2.5	2.79 ± 0.10

Equation (5) predicts the value 3.80 for the scaled slope of the stress–strain curve  $\frac{1}{\sigma} \frac{d\sigma}{d\epsilon}$  at 50% compression. The experimental values in the last column can be compared with this prediction

**Table 3** Basic material properties of the foam-formed materials with added fine components

TP#	Fine component	Density (kg/m <sup>3</sup> )	Stress (kPa, 10%)	Stress (kPa, 50%)	$\frac{1}{\sigma} \frac{d\sigma}{d\epsilon}$ at 50%
7	No added fine components	48.6	3.3 ± 0.5	21.0 ± 2.7	4.52 ± 0.19
8	V-fines (10%)	44.3	5.4 ± 0.4	27.4 ± 1.0	4.00 ± 0.14
9	CMF (10%)	45.8	6.9 ± 0.8	34.4 ± 2.0	3.86 ± 0.18
10	TCNF (10%)	51.5	8.1 ± 0.9	42.2 ± 4.7	3.88 ± 0.15
11	V-fines (10%) and LBG (25%)	38.5	17.1	37.4	3.52

In all cases, the furnish was unrefined NBSK (80%) and hemp fibres (20%) with 1% addition of cationic starch, and the surfactant was SDS. The added fine component amounts are given as a weight proportion of the fibre component (NBSK + hemp, 100%). Equation (5) predicts the value 3.80 for the scaled slope of the stress–strain curve  $\frac{1}{\sigma} \frac{d\sigma}{d\epsilon}$  at 50% compression. The experimental values in the last column can be compared with this prediction. There is no error estimate for the special LBG trial point TP11 because of a lack of parallel samples in this case

distributed segment lengths (Sampson 2008; Subramanian and Picu 2011), and that the changes in mean supporting structural element follow the macroscopic strain. In such a case, the material stress  $\sigma(\epsilon)$  at the compressive strain  $\epsilon$  can be written as

$$\sigma(\epsilon) = \frac{\sigma_0}{[s(\epsilon)]^2}, \quad (1)$$

$$[s(\epsilon) + 1]e^{-s(\epsilon)} = \epsilon \quad (2)$$

where the function  $s(\epsilon)$  describes the mean relative length of fibre segments that buckle at strain  $\epsilon$ , and  $\sigma_0$  is a constant corresponding to the stress at strain  $\epsilon_1 = 2e^{-1}$  at which  $s(\epsilon) = 1$ . In other words, the constant  $\sigma_0$  sets the absolute level of compression stress, which depends not only on the fibre type but also on bonding properties. According to the theory, load–displacement behaviour is described by the same function  $s(\epsilon)$

for all random fibre networks with exponentially distributed segment lengths. The mean-field argument used to derive Eqs. (1, 2) is geometric, and bucklings are used only to connect local deformations with the applied stress. Thus, deriving the equations does not require any assumption on the proportion of fibre segments that undergo buckling nor on their post-buckling behaviour. However, the acoustic emission measurements by Mäkinen et al. (2020) indicate that a significant amount of acoustic energy during compression is released by events whose number is described explicitly by the function  $s$  defined by Eq. (2).

In an earlier study (Ketoja et al. 2019), the buckling theory predicted the quantitative compression behaviour surprisingly well for the studied fibre materials. This was seen by comparing the prediction of Eq. (1) with experimental compression–stress curves and



considering the statistical distribution of the ratio of stresses measured at 50% and 10% compression levels with a theoretical prediction,

$$\frac{\sigma(0.5)}{\sigma(0.1)} = \left[ \frac{s(0.1)}{s(0.5)} \right]^2 \approx 5.374 \quad (3)$$

In reality, other deformation modes like the bending of fibres can be significant as well (Hossain et al. 2019; Bergström et al. 2019). Moreover, especially the initial deformation behaviour can be very non-uniform (Mäkinen et al. 2020). However, Eqs. (1, 2) provide an interesting reference curve which helps the comparison of the data. In the current study, we consider the slope of the stress–strain curve at high strain levels,

$$\frac{d\sigma(\epsilon)}{d\epsilon} = \frac{2\sigma_0 e^{s(\epsilon)}}{[s(\epsilon)]^4} = \frac{2\sigma(\epsilon)[s(\epsilon) + 1]}{\epsilon[s(\epsilon)]^2} \quad (4)$$

instead of the ratio given by Eq. (3). This slope is less sensitive to the changes at small strains, which are poorly described by the simplified model lacking the effect of fibre bending or closing up of large initial voids at small strains. At 50% compression, we obtain the prediction

$$\frac{1}{\sigma} \frac{d\sigma}{d\epsilon} (\epsilon = 0.5) = \frac{4[s(0.5) + 1]}{[s(0.5)]^2} \approx 3.804 \quad (5)$$

for the slope of the stress–strain curve scaled by the stress level. We will compare this value with the corresponding experimental results in addition to plotting the complete stress–strain curves against the theoretical Eq. (1).

## Results and discussion

### Effects of fibre size distribution and the type of foaming agent

The foam-formed fibre materials differ significantly from conventional water-formed random fibre networks. Perhaps, the most striking feature is the significant proportion of large pores, which are left as traces of air bubbles. This is seen clearly in the x-ray scans of the fibre network, viewed over a series of planar sections in the thickness direction (see Supplementary material). The traces are not as clear in the cross-sectional side views because of the partial collapse of the pores during the density adjustment.

Still, the overall pore size distribution is affected by the mean bubble size also in denser foam-formed sheets than those studied here (Al-Qararah et al. 2015b).

The above bubble traces cause the material distribution to be heterogeneous in the micro scale so that fibres are confined in narrow gaps between bubbles. Thus, the effective local density can become quite large in these densified regions. This has an important impact on the compression properties of the materials. Besides the normal pores, almost all samples included also larger voids, which may have originated from either very big bubbles or local opening of the fibre network because of drying stresses. The other typical heterogeneity came from the denser material surfaces, which was caused by the rewetting and pressing procedure used in sample making.

Table 2 shows the measured initial material density and compression stress at two deformation levels, 10% and 50%, for the various trial points without added fine components. We expect the structure to become more uniform when the compression proceeds and possible voids are closed. Therefore, it is of interest to compare the slope of the stress–strain curve at the highest studied compression level (50%) with the theoretical prediction. This comparison is also included in Table 2.

Compression stress (see Fig. 6a) and especially the compression modulus (see Fig. 6b) increased when polymeric water-soluble and film-forming PVA was applied as the foaming agent instead of anionic SDS. The refining of NBSK, which caused external fibrillation of the fibres and the generation of cellulosic fines, increased the relative material strength of the PVA foamed samples (TP5) more than the strength of the SDS foamed samples (TP2). Despite material non-uniformity (see Fig. 7b), PVA increased bonding so that both types of fibres, as well as formed cellulosic fines, contributed more actively to the strength of a highly porous fibre network. The material may have densified locally because of the large voids in the material obtained using PVA, see Fig. 7b. Subsequently, the mean free segment length in the fibre network was shorter in the densified regions. This could make a significant contribution to strength, which behaves like the square of density in these types of materials (Ketoja et al. 2019). The effect of improved bonding was seen, especially when 20% of the refined NBSK pulp was replaced with poorly

bonding but stiff and long hemp fibres. The compression stress and modulus of the PVA trial point were further improved with the addition of hemp (TP6). In contrast, a slight drop in these properties was seen for the SDS trial point (TP3) where fibres distributed more evenly and the local densification was not as strong, see Fig. 7a.

When looking at the stress–strain curves of Fig. 8, the refined and unrefined NBSK samples obtained with SDS follow the predicted theoretical behaviour (Ketoja et al. 2019) of random fibre networks [refer to Eqs. (1, 2)] quite well, except below 10% strain (Mäkinen et al. 2020). A slight deviation was observed with the added hemp component in Fig. 8c, which could have resulted from either voids in the structure or altered fibre segment distribution for intermediate span lengths. Interestingly, similar compression–stress behaviour was produced by unrefined NBSK with the PVA foaming agent (see Fig. 8d), which produced an uneven fibre network with large voids (Fig. 7b). It is possible that PVA forms films (Bossu et al. 2019) that, together with increased bonding and locally increased density, interfere with the distribution of intermediate segment lengths in a fashion similar to when refining and hemp are added. The deviation from the model behaviour for the PVA samples appeared to increase with NBSK refining (Fig. 8e) and added hemp component (Fig. 8f). Both factors probably drove the formed complex multi-scale material network away from the simple random fibre network that had exponentially distributed free segment lengths. The scaled slope of stress–strain curve  $\frac{1}{\sigma} \frac{d\sigma}{d\epsilon}$  at 50% compression, when the large voids can be expected to be closed, varies in the range of 2.8–4.4, see Table 2. All

results with SDS surfactant are relatively close (average deviation 9%) to the theoretical prediction 3.8 given by Eq. (5). The larger deviations from the theory with PVA foaming agent for refined NBSK cause a clear drop in the slope at 50% compression.

Buckling of fibre segments has been postulated as the failure mechanism underlying Eqs. (1, 2) (Ketoja et al. 2019; Mäkinen et al. 2020). Thus, the recovery of sample thickness after the load has been removed should depend mainly on the recovery of fibres from buckling deformation and not on bonding properties. Figure 9 shows the thickness recovery of samples exposed to 50% compression recorded 1 min after the load was removed. The recovery was roughly equal for both surfactant types despite their highly different bonding properties. This agrees with the above theoretical postulate. Unrefined curly Kraft fibres led to better recovery than straighter refined Kraft fibres. Addition of hemp fibres (TP3 and TP6) did not change this picture.

#### Effects of lignocellulosic fines, cellulose nanofibrils, and LBG

The results presented in the previous chapter suggest that the fines and fibrillation coming from refining, together with added strengthening polymers like PVA, can “activate” the multi-scale fibre network and improve strength properties significantly. Thus, the contribution to strength of fines, fibrils, and macromolecules was studied more thoroughly. This was done for the fibre composition that included 80% NBSK and 20% long hemp pulp fibres. The testing plan (see Table 3) included the reference with starch

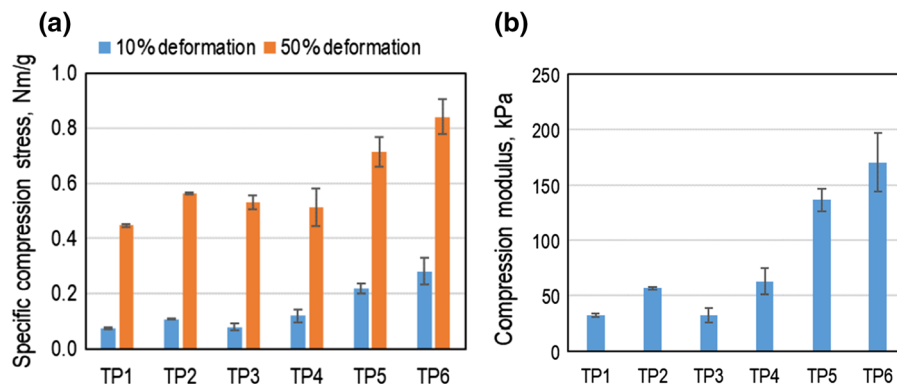


**Fig. 6** **a** Specific compression stress (compression stress divided by bulk density) of the materials (Table 2) made with SDS (TP1–3) and PVA (TP4–6) foams at 10% and 50% deformation. **b** The compression modulus of the same materials

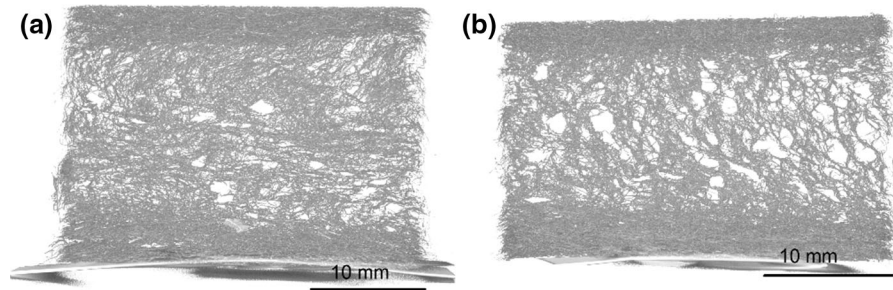


**Fig. 7** Typical cross-sectional images obtained with x-ray tomography for **a** refined NBSK and hemp with SDS (TP3), and **b** unrefined NBSK with PVA (TP4). Both samples include voids which cause deviation from the theoretical stress–strain curve

below 40% strain in Fig. 8c, d. The images are averages of 60 slices taken from a central part of the samples. Wire side is at the bottom

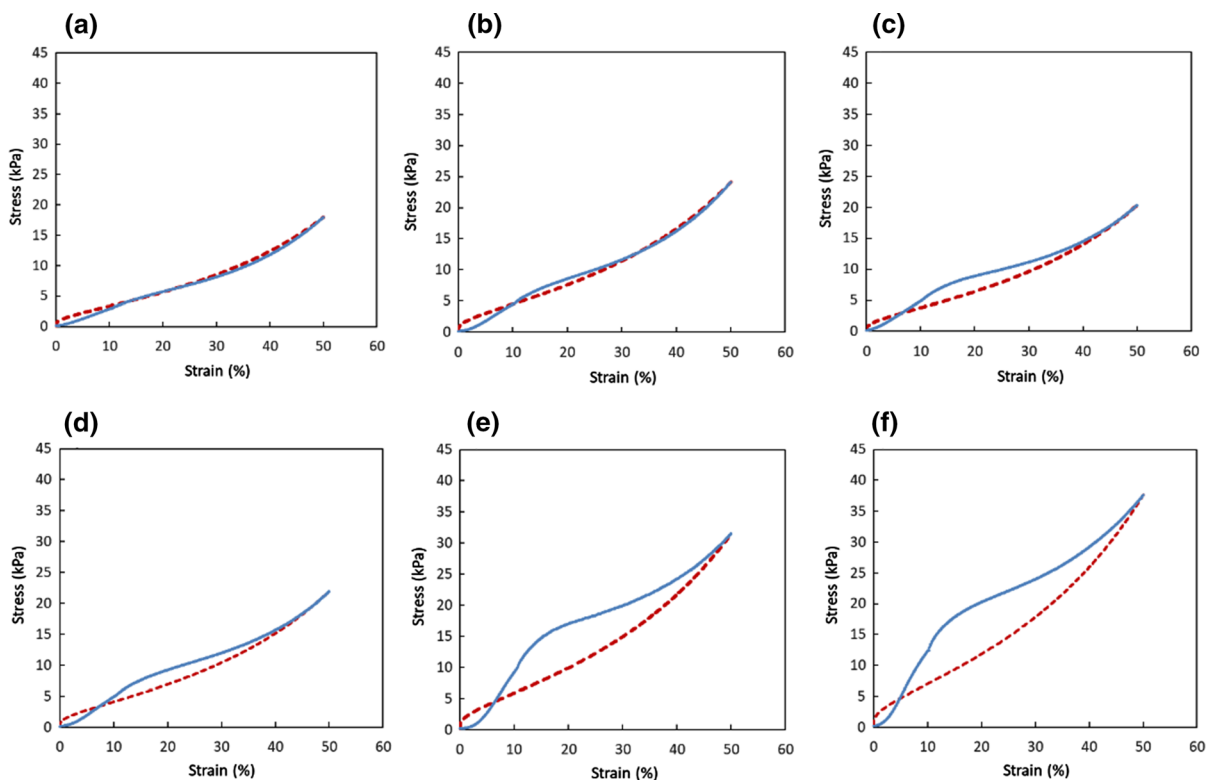


**Fig. 8** Comparison of the measured compression behaviour (solid curve) to the theoretical prediction (dashed curve) for **a** unrefined Kraft (TP1), **b** refined Kraft (TP2), **c** refined Kraft and hemp (TP3), **d** unrefined Kraft and PVA (TP4), **e** refined Kraft and PVA (TP5), and **f** refined Kraft, hemp, and PVA (TP6). The

experimental stress–strain curves are averages of 5 parallel measurements from the 1st (0–10%) and 2nd (10–50%) cycles. The foaming agent was SDS for the data in **a–c**. The parameter  $\sigma_0$  of Eq. (1) was fitted to the experimental curve at 50% strain

(TP7), and the trial points with added V-fines (TP8), CMF (TP9) and TCNF (TP10). The addition of fine components was 10% of the long fibre amount. Cationic starch was added to ensure high retention of the negatively charged fibrils. Retention of the fine

materials was not measured. However, based on the work of Turpeinen et al. (2018) and the realized grammages, we assume high, over 90% retention. This trial set was extended with a special trial point that included a partly soluble natural polymer, colloidal

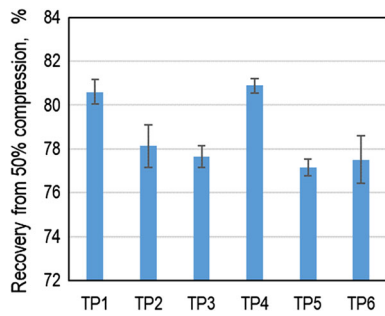


**Fig. 9** Recovery from 50% compression 1 min after the load was removed. The recovery depended more on the fibre properties than on network bonding. TP1–3 are samples made with SDS and TP4–6 samples made with PVA foam

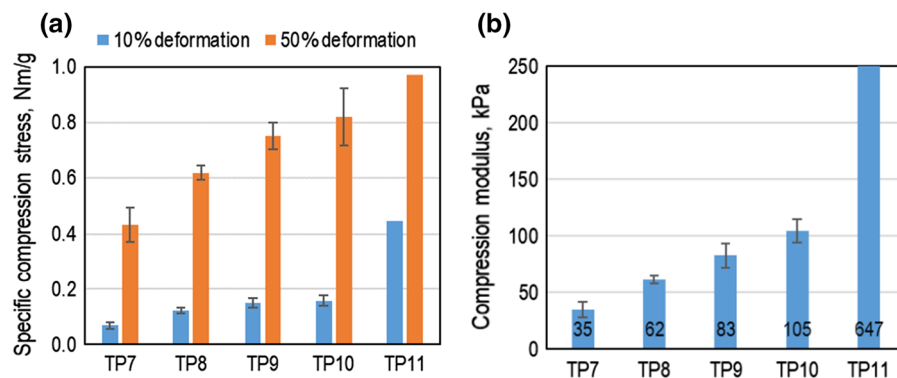
LBG (TP11) with addition level of 25% of the long fibre amount. With its high molecule weight, this component could be viewed to describe the bonding behaviour for an additive having size scale between PVA and TCNF. Assuming complete retention, the amounts of fine components (V-fines, CMF, and TCNF) and LBG in the whole material were 7% and 18%, respectively. Table 3 shows the measured material properties with densities varying in the range of 38–51 kg/m<sup>3</sup>.

The addition of fine components caused an apparent increase in all the measured strength properties, as shown in Fig. 10. Within experimental accuracy, the finest and highly charged TCNF did not increase compression stress much more than CMF. The clearly coarsest fine component, fibrillar V-fines, also had potential as a strength additive. The addition of LBG clearly led to the highest compression modulus and compression stress at the small 10% deformation level (see Fig. 10). The formed material was very hard and

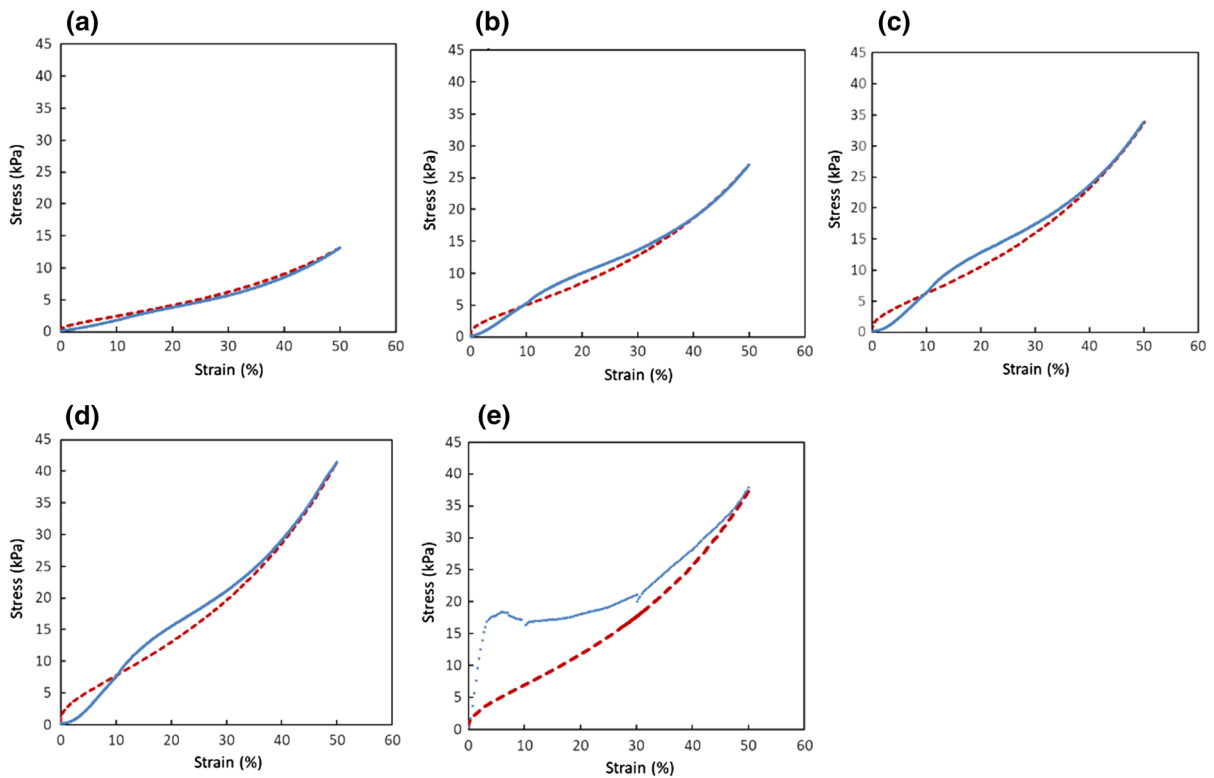
brittle so that the fractures formed at higher compressive strains caused a decay of the compression stress. At small strains, the addition of LBG or similar hydrocolloidal natural polysaccharide can improve the strength and stiffness of fibre foams made with SDS tremendously. Values that are similar to or improved compared with foaming with PVA can be achieved.

Figure 11 shows the stress–strain behaviour for unrefined kraft and hemp with added fine components. Earlier without added fines, this furnish (TP3) led to significant deviation from the theoretical behaviour of Eqs. (1, 2) at strains below 40% (Fig. 8c). Curiously, with added fine components, the agreement was much better over the whole strain range of 10–50%, as shown in Fig. 11b–d. The same was observed with added cationic starch (Fig. 11a). As shown by Fig. 12, both the fine components and the starch made the network more uniform and tightly bonded, which might have brought the distribution of segment lengths closer to the assumed exponential distribution of the theoretical model. The same theoretical form was well maintained, even when the fitted factor  $\sigma_0$  of Eq. (1) increased significantly when finer particles were used. This increase was probably at least partly caused by the higher local density (Ketoja et al. 2019) achieved with more effective bonding.

In Table 3, the scaled slope of stress–strain curve  $\frac{1}{\sigma} \frac{d\sigma}{d\epsilon}$  at 50% compression varies in the range of 3.5–4.5. Thus, the deviation from the theoretical value 3.8 is rather small. Moreover, the experimental slope is not correlated with material density (also compare with Table 2). Similar quantitative agreement was observed with a broader range of densities earlier (Ketoja et al. 2019). A correlation with material



**Fig. 10** **a** Specific compression stress at 10% and 50% deformation, and **b** compression modulus for the samples with added fine components (Table 3). Note that the modulus obtained with added LBG exceeded the scale of the y-axis



**Fig. 11** Comparison of the measured compression behaviour (solid curve) to the theoretical prediction (dashed curve) for structures made with unrefined Kraft (80%) and hemp (20%) with **a** cationic starch, **b** V-fines and starch, **c** CMF and starch, **d** TCNF and starch. The experimental stress–strain curves are

averages of 5 parallel measurements from the 1st (0–10%) and 2nd (10–50%) cycles. The last figure **e** shows the plot for the special LBG trial point TP11. The foaming agent was SDS for all samples

density would be expected if the stress increase at high compression was caused mainly by the appearance of new inter-fibre contacts as proposed earlier (Ali-madadi et al. 2018). With higher initial density, the proposed densification mechanism should take place earlier during compression, and the scaled slope at 50% compression should increase with initial density. Our data does not support this idea for the compression levels studied. Even at 50% compression, densities of the studied materials are still rather low, and the mean contact stress (Subramanian and Picu 2011) remains small.

## Conclusions

The mechanical behaviour of foam-formed light-weight materials can be greatly affected by the multi-scale raw material components chosen, even

when the density of the final dried materials is kept on a similar level. Interestingly, the most significant impacts were from the smallest polymer components, such as the PVA and LBG. Using PVA to make wet foam leads to an uneven fibre network but to a stronger material than the one obtained using SDS foam. PVA densified the network locally and formed a film sub-structure, which affected fibre segment buckling. This was visible as a deviation from the theoretical stress–strain curve based on exponentially distributed segment lengths. A similar deviation was observed when hemp bast fibres that bonded poorly with NBSK were added. On the other hand, after improving bonding and material homogeneity with fine components, the experimental stress–strain curves approached the theoretical prediction in all cases with the SDS surfactant beyond 40% strain. Among all studied samples, the average scaled slope of the stress–strain curve at 50% compression was  $3.79 \pm 0.33$ , which

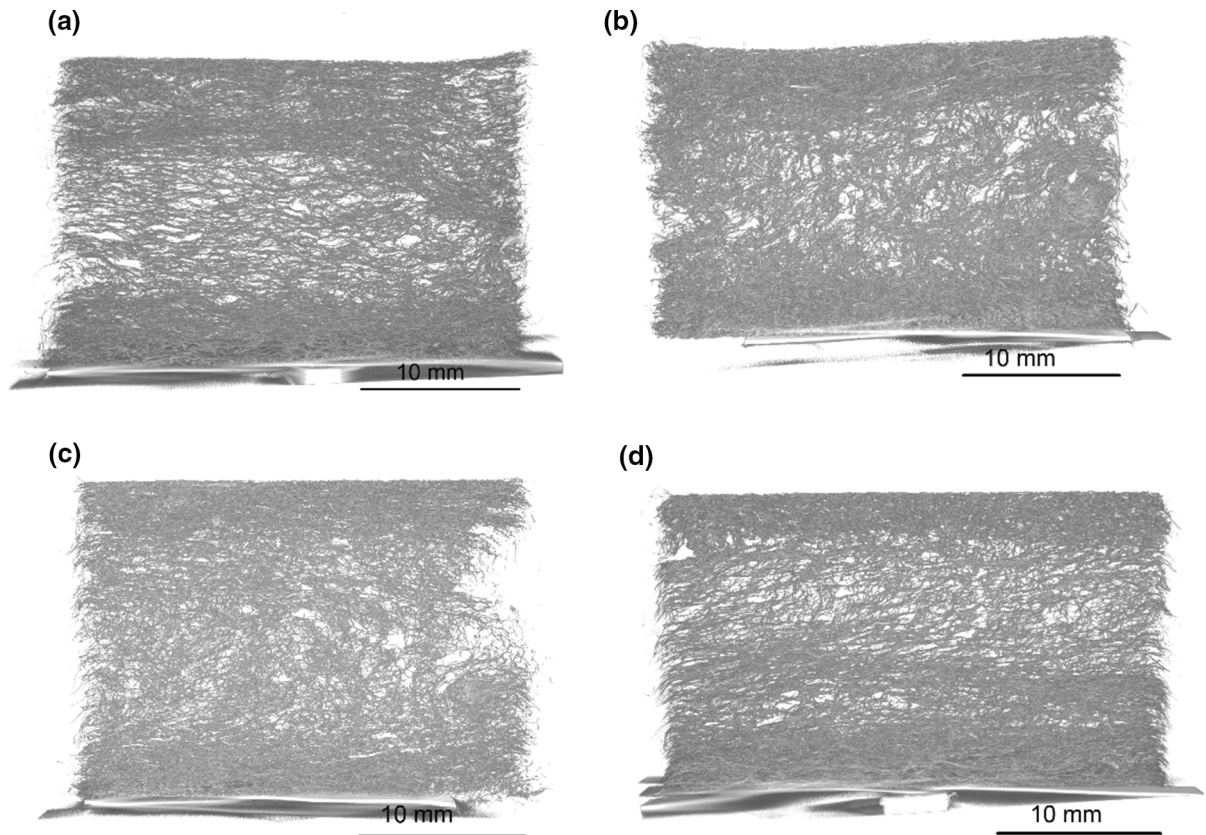


**Fig. 12** Typical cross-sectional images obtained with x-ray tomography for samples with fine components. **a** Reference with unrefined NBSK and hemp with starch (TP7). The added fine

components included **b** V-fines (TP8), **c** CMF (TP9), and **d** TCNF (TP10). The corresponding stress–strain curves are shown in Fig. 11. Wire side is at the bottom

can be compared with theoretical prediction of 3.80. Moreover, the slope was not correlated with material density. This gives further evidence of a buckling mechanism describing the observed stress–strain behaviour at intermediate compression levels, before collective phenomena soften the structure (Mäkinen et al. 2020).

The resilience of the samples after compression was not affected by the bonding properties but by the dominant fibre type. This suggests that resilience is related to the recovery of fibres from earlier buckling; poor resilience does not necessarily mean that inter-fibre bonds would have failed.

These findings will be useful in developing new applications for lightweight cellulose materials, where separate tuning of mechanical behaviour and material density are essential.

**Acknowledgments** Open access funding provided by Technical Research Centre of Finland (VTT). This article was based on the results achieved in the Novel Structural Materials with Multi-scale Fibre Components (NoMa) project. The authors are grateful for the financial support from Tekes (now Business Finland, the Finnish innovation funding, trade, investment, and travel promotion organization), VTT, the participating companies, and Lahti University of Applied Sciences. We are also grateful for the support by the FinnCERES Materials Bioeconomy Ecosystem. We would like to thank Kirsi Immonen and Jari Sirviö for useful discussions. Tuomas Turpeinen, Annika Ketola, Päivi Sarja, Meiju Sinkkonen, and Timo Rantanen are appreciated for their laboratory and analysis work.

**Funding** Funding was provided by Tekes and VTT.

**Compliance with ethical standards**

**Conflict of interest** The authors declare that they have no conflicting interests.

**Open Access** This article is licensed under a Creative Commons Attribution 4.0 International License, which permits use, sharing, adaptation, distribution and reproduction in any medium or format, as long as you give appropriate credit to the original author(s) and the source, provide a link to the Creative Commons licence, and indicate if changes were made. The images or other third party material in this article are included in the article's Creative Commons licence, unless indicated otherwise in a credit line to the material. If material is not included in the article's Creative Commons licence and your intended use is not permitted by statutory regulation or exceeds the permitted use, you will need to obtain permission directly from the copyright holder. To view a copy of this licence, visit <http://creativecommons.org/licenses/by/4.0/>.

## References

- Alava M, Niskanen K (2006) The physics of paper. *Rep Prog Phys* 69:669–723
- Alimadadi M, Uesaka T (2016) 3D-oriented fiber networks made by foam forming. *Cellulose* 23(1):661–671
- Alimadadi M, Lindström SB, Kulachenko A (2018) Role of microstructures in the compression response of three-dimensional foam-formed wood fibre networks. *Soft Matter* 14:8945–8955
- Al-Qararah AM, Hjelt T, Koponen A, Harlin A, Ketoja JA (2015a) Response of wet foam to fibre mixing. *Colloids Surf A Physicochem Eng Asp* 467:97–106
- Al-Qararah AM, Ekman A, Hjelt T, Ketoja JA, Kiiskinen H, Koponen A, Timonen J (2015b) A unique microstructure of the fiber networks deposited from foam-fiber suspensions. *Colloids Surf A Physicochem Eng Asp* 482:544–553
- Barak S, Mudgil D (2014) Locust bean gum: processing, properties and food applications—a review. *Int J Biol Macromol* 66:74–80
- Bergström P, Hossain S, Uesaka T (2019) Scaling behavior of strength of 3D-, semi-flexible-, cross-linked fibre network. *Int J Solids Struct* 166:68–74
- Bossu J, Eckhart R, Czibula C, Winter A, Zankel A, Gindl-Altmutter W, Bauer W (2019) Fine cellulosic materials produced from chemical pulp: the combined effect of morphology and rate of addition on paper properties. *Nanomaterials* 9(3):321
- Burke SR, Möbius ME, Hjelt T, Hutzler S (2019) Properties of lightweight fibrous structures made by a novel foam forming technique. *Cellulose* 26(4):2529–2539
- EN 826 (2013) Thermal insulating products for building applications—determination of compression behaviour
- Finch CA (ed) (1992) *Polyvinyl alcohol—developments*. Wiley, London
- Hossain MS, Bergström P, Uesaka T (2019) Uniaxial compression of three-dimensional entangled fibre networks: impacts of contact interactions. *Model Simul Mater Sci Eng* 27:015006
- Jahangiri P, Korehei R, Zeinoddini SS, Madani A, Sharma Y, Phillion A, Martinez DM, Olson JA (2014) On filtration and heat insulation properties of foam formed cellulose based materials. *Nord Pulp Pap Res J (Biorefinery)* 29(4):584–591
- Jahangiri P, Logawa B, Korehei R, Hodgson M, Martinez DM, Olson JA (2016) On acoustical properties of novel foam-formed cellulose-based material. *Nord Pulp Pap Res J* 31(1):14–19
- Järvinen M, Pihko R, Ketoja JA (2018) Density development in foam forming: wet pressing dynamics. *Nord Pulp Pap Res J* 33:226–236
- Ketoja JA, Paunonen S, Jetsu P, Pääkkönen E (2019) Compression strength mechanisms of low-density fibrous materials. *Materials* 12:384
- Komori T, Makishima K (1977) Numbers of fiber-to-fiber contacts in general fiber assemblies. *Text Res J* 47:13–17
- Lahtinen P, Liukkonen S, Pere J, Sneck A, Kangas HA (2014a) Comparative study of fibrillated fibers from different mechanical and chemical pulps. *BioResources* 9(2):2115–2127
- Lahtinen P, Torvinen K, Kangas H, Liukkonen S, Sneck A, Peresin MS, Pere J, Hänninen T, Meyer V, Tammelin T (2014b) Effect of fibrillated cellulosic additives on paper strength properties. In: *PaperCON 2014 proceedings*, TAPPI
- Luo Y, Xiao S, Li S (2017) Effect of initial water content on foaming quality and mechanical properties of plant fibre porous cushioning materials. *BioResources* 12(2):4259–4269
- Madani A, Zeinoddini S, Varahmi S et al (2014) Ultra-light-weight paper foams: processing and properties. *Cellulose* 21:2023–2031
- Mäkinen T, Koivisto J, Pääkkönen E, Ketoja JA, Alava MJ (2020) Crossover from mean-field compression to collective phenomena in low-density foam-formed fiber material. *Soft Matter* (**submitted**)
- Miller GD, Boylan JR, Jones RB (1998) Synthetic coating adhesives. Poly(vinyl alcohol)—a versatile polymer for paper and paperboard applications. Tappi Press
- Neagu C, Gamstedt K, Berthold F (2006) Stiffness contribution of various wood fibers to composite materials. *J Compos Mater* 40:663–699
- Nurminen I, Saharinen E, Sirviö J (2018) New technology for producing fibrillar fines directly from wood. *BioResources* 13(3):5032–5041
- Paunonen S, Timofeev O, Torvinen K, Turpeinen T, Ketoja JA (2018) Improving compression recovery of foam-formed fiber materials. *BioResources* 13:4058–4074
- Picu RC (2011) Mechanics of random fiber networks—a review. *Soft Matter* 7:6768–6785
- Picu RC, Subramanian G (2011) Correlated heterogeneous deformation of entangled fiber networks. *Phys Rev E* 84(3):031904
- Pöhler T, Jetsu P, Isoimoisio H (2016) Benchmarking new wood-fibre based sound absorbing material made with a foam-forming technique. *Build Acoust* 23(3–4):131–143
- Pöhler T, Jetsu P, Fougeron A, Barraud V (2017) Use of papermaking pulps in foam-formed thermal insulation materials. *Nord Pulp Pap Res J* 32(3):367–374
- Poranen J, Kiiskinen H, Salmela J, Asikainen J, Keränen J, Pääkkönen E (2013) Breakthrough in papermaking resource efficiency with foam forming. In *Proceedings of the TAPPI PaperCon*, Atlanta, GA, 28 April–1 May 2013

- Sampson WW (2008) Unified theory for structural statistics of flocculated and random fibre networks. *J Pulp Pap Sci* 34:91–98
- Schmied FJ, Teichert C, Kappel L, Hirn U, Bauer W, Schennach R (2013) What holds paper together: nanometre scale exploration of bonding between paper fibres. *Sci Rep* 2013:3
- Shahzad A (2012) Hemp fiber and its composites—a review. *J Compos Mater* 46(8):973–986
- Skogberg A, Mäki A-J, Mettänen M, Lahtinen P, Kallio P (2017) Cellulose nanofiber alignment using evaporation-induced droplet—casting and cell alignment on aligned nanocellulose surfaces. *Biomacromol* 18:3936–3953
- Sormunen T, Ketola A, Miettinen A, Parkkonen J, Retulainen E (2019) X-ray nanotomography of individual pulp fibre bonds reveals the effect of wall thickness on contact area. *Sci Rep* 9:4258
- Subramanian G, Picu CR (2011) Mechanics of three-dimensional, nonbonded random fiber networks. *Phys Rev E* 83:056120
- Turpeinen T, Lappalainen T, Kenttä E, Torvinen K (2018) Detection of iron and iron-cobalt labeled cellulose nanofibrils using ICP-OES and X $\mu$ CT. *Nord Pulp Pap Res J* 33(4):610–617

**Publisher's Note** Springer Nature remains neutral with regard to jurisdictional claims in published maps and institutional affiliations.